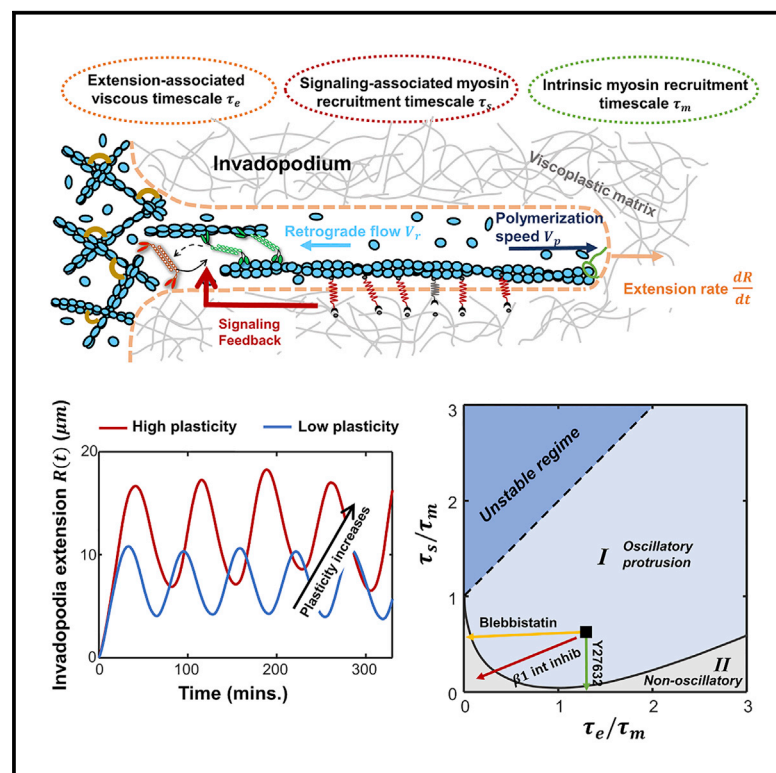# Recursive feedback between matrix dissipation and chemo-mechanical signaling drives oscillatory growth of cancer cell invadopodia

Graphical abstract

Authors

Ze Gong, Katrina M. Wisdom, Eóin McEvoy, ..., Christopher C. Price, Ovijit Chaudhuri, Vivek B. Shenoy

Correspondence

vshenoy@seas.upenn.edu

In brief

Gong et al. develop a chemo-mechanical model to predict the impact of matrix plasticity on invadopodia dynamics by considering myosin recruitment, actin polymerization, and mechano-sensitive signaling. The combined experiments and simulations show that invadopodia oscillate when timescales for extension and myosin dynamics are comparable, and high matrix plasticity facilitates the oscillations.

Highlights

- A chemo-mechanical model for invadopodia dynamics in 3D matrices is developed

- Oscillations occur when timescales for extension and myosin dynamics are comparable

- Matrix plastic strain accumulates by cyclic ratcheting during invadopodia growth

- High matrix plasticity facilitates the oscillatory growth of invadopodia

Cell Reports

Article

Recursive feedback between matrix dissipation and chemo-mechanical signaling drives oscillatory growth of cancer cell invadopodia

Ze Gong,[1,2] Katrina M. Wisdom,[2,3,4] Eóin McEvoy,[1,2] Julie Chang,[5] Kolade Adebowale,[6] Christopher C. Price,[1] Ovijit Chaudhuri,[3] and Vivek B. Shenoy[1,2,7,*]
[1]Department of Materials Science and Engineering, University of Pennsylvania, Philadelphia, PA 19104, USA
[2]Center for Engineering Mechanobiology, University of Pennsylvania, Philadelphia, PA 19104, USA
[3]Department of Mechanical Engineering, Stanford University, Stanford, CA 94305, USA
[4]Department of Bioengineering, University of Pennsylvania, Philadelphia, PA 19104, USA
[5]Department of Bioengineering, Stanford University, Stanford, CA 94305, USA
[6]Department of Chemical Engineering, Stanford University, Stanford, CA 94305, USA
[7]Lead contact
*Correspondence: vshenoy@seas.upenn.edu
https://doi.org/10.1016/j.celrep.2021.109047

SUMMARY

Most extracellular matrices (ECMs) are known to be dissipative, exhibiting viscoelastic and often plastic behaviors. However, the influence of dissipation, in particular mechanical plasticity in 3D confining microenvironments, on cell motility is not clear. In this study, we develop a chemo-mechanical model for dynamics of invadopodia, the protrusive structures that cancer cells use to facilitate invasion, by considering myosin recruitment, actin polymerization, matrix deformation, and mechano-sensitive signaling pathways. We demonstrate that matrix dissipation facilitates invadopodia growth by softening ECMs over repeated cycles, during which plastic deformation accumulates via cyclic ratcheting. Our model reveals that distinct protrusion patterns, oscillatory or monotonic, emerge from the interplay of timescales for polymerization-associated extension and myosin recruitment dynamics. Our model predicts the changes in invadopodia dynamics upon inhibition of myosin, adhesions, and the Rho-Rho-associated kinase (ROCK) pathway. Altogether, our work highlights the role of matrix plasticity in invadopodia dynamics and can help design dissipative biomaterials to modulate cancer cell motility.

INTRODUCTION

Cancer cells invade extracellular matrices (ECMs) from primary tumors and intravasate into circulation in order to metastasize to distal organs. During this process, cells can actively modify their spreading (Chaudhuri et al., 2015; Discher et al., 2005; Vogel and Sheetz, 2006) and migration (Pakshir et al., 2019; Sunyer et al., 2016; van Helvert et al., 2018) by sensing the ECM's mechanical properties, including stiffness (Chan and Odde, 2008; Discher et al., 2005; Elosegui-Artola et al., 2014) and viscosity (Bennett et al., 2018; Charrier et al., 2018; Chaudhuri et al., 2020; Gong et al., 2018). Such mechano-sensitivity is thought to be governed by adhesion dynamics and actomyosin contractility, and several approaches have been developed to quantitatively study mechano-transduction processes, including motor clutch dynamics for adhesions (Chan and Odde, 2008; Prahl et al., 2020) and chemo-mechanical feedback models for contractility (Alisafaei et al., 2019; Shenoy et al., 2016). Beyond stiffness and viscosity, certain ECMs, such as reconstituted basement membrane (rBM) matrices and type I collagen gels, exhibit plastic behavior, in which deformation can be irreversible (Ban et al., 2018; Nam et al., 2016).

Recent studies have shown that invadopodia, which are actin-rich protrusions, can deform viscoplastic ECMs to facilitate invasive cell migration through matrices by mechanical force alone, independent of proteases (Wisdom et al., 2018; Wisdom et al., 2020). As these viscoplastic ECMs can be permanently deformed and thus possess long-term mechanical memory, how cells are able to sense plastic deformation and modify their behavior is a crucial, but as yet unanswered, question.

Live imaging studies have revealed the dynamics of invadopodia assembly (Artym et al., 2006; Murphy and Courtneidge, 2011; Oser et al., 2009; Sibony-Benyamini and Gil-Henn, 2012) as well as the oscillatory growth and retraction cycles of these invasive protrusions (Enderling et al., 2008; Pourfarhangi et al., 2018). While many of these studies have focused on cells plated on two-dimensional (2D) substrates, there is a growing appreciation that invadopodia in 3D environments can evolve into more elongated mature structures compared to those in 2D (Génot and Gligorijevic, 2014; Tolde et al., 2010). In highly plastic 3D environments, Wisdom et al. (2018) recently observed that oscillations of elongated invadopodia protrusions allow cells to migrate through pores. Invadopodia oscillatory growth also suggests
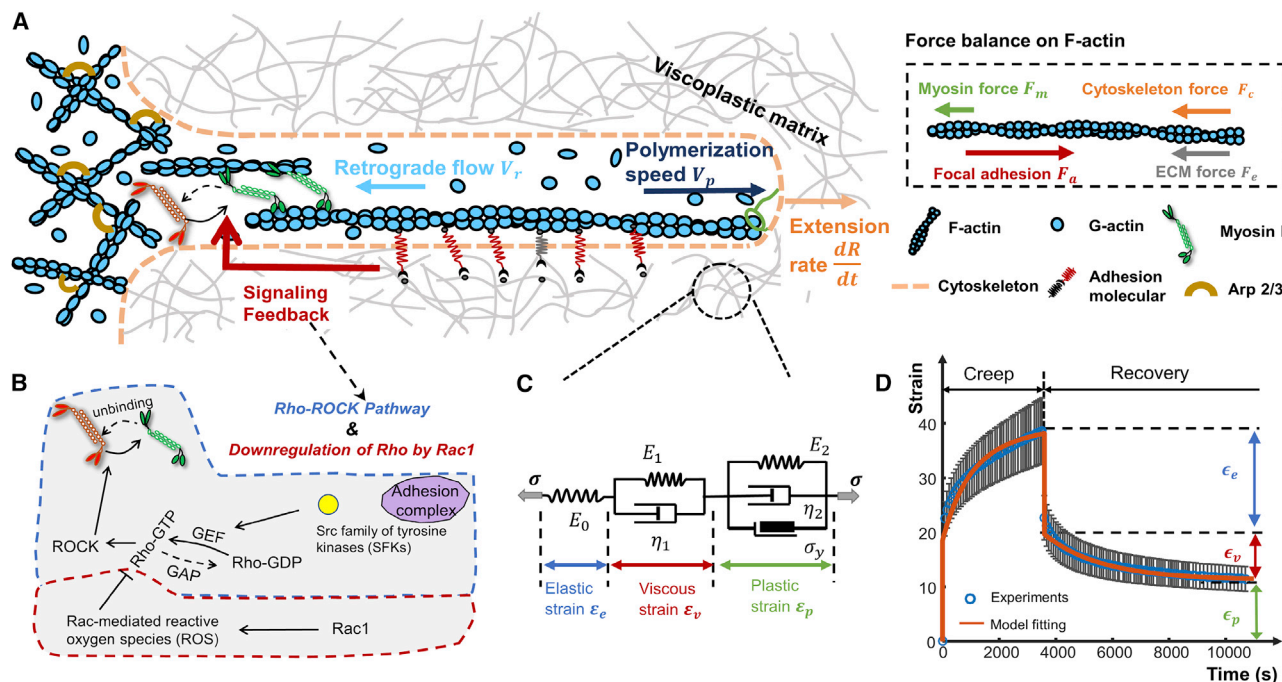
Figure 1. A chemo-mechanical model that integrates the balance of mechanical forces and mechano-sensitive signaling pathways

(A) Schematic describing the model for invadopodia protrusion. Myosin motors pull actin filament bundles toward the cell center with retrograde flow velocity V_r. Adhesion molecules, connecting actin bundles to the extracellular matrix (ECM), provide a frictional force to resist retrograde flow. Actin monomers are polymerized at the tip of filament bundles (with polymerization speed V_p) against the viscoelastic cortical cytoskeleton and viscoplastic ECM forces. The invadopodia extension rate dR/dt is the difference between polymerization speed V_p and retrograde flow V_r.

(B) Mechano-sensitive signaling pathways that influence dynamics of myosin recruitment. Tensile forces at the adhesion complex trigger a conformation change of vinculin, exposing binding sites of the Src family of tyrosine kinases (SFKs). SFKs promote Rho-GTPases by controlling the activity of guanine nucleotide exchange factors (GEFs) and GTPase-activating proteins (GAPs), which increases the binding of myosin motors. Rho-GTPases are downregulated by Rac1 kinases through Rac-mediated reactive oxygen species (ROS).

(C) The mechanical model with elastic, viscous, and plastic components for viscoplastic matrices.

(D) The creep-recovery test showing the presence of irreversible strain (ε_p) after recovery of stress in the ECM. The constitutive law is obtained by fitting a viscoplastic model (red line) to experimental data (blue circles). Data are shown as mean ± SD for nine individual tests.

that cells can sense the dissipative properties (i.e., viscoelasticity and viscoplasticity) of ECMs, as they deform ECMs in a time-dependent manner. However, the mechanism of how different intracellular processes cooperate, interact with extracellular space, and lead to oscillatory growth remains unclear.

To obtain biophysical insights into these phenomena, we propose a chemo-mechanical model that considers the interactions between multiple intracellular processes (including adhesion dynamics, actin polymerization, myosin recruitment, and mechano-sensitive signaling pathways) and the deformation of ECMs. Our model reveals how the interplay of characteristic timescales of extension-associated viscosity, intrinsic myosin recruitment, and signaling-associated myosin recruitment leads to oscillatory versus monotonic growth of invadopodia in 3D confining microenvironments. By using recently developed viscoplastic interpenetrating network (IPN) hydrogels (Wisdom and Chaudhuri, 2017; Wisdom et al., 2018), we experimentally assess our model predictions for different levels of matrix plasticity and pharmacological inhibitors. The mechanistic understanding of invadopodia dynamics obtained here can be used to gain insight on mechanisms of invasion during the early stages of cancer metastasis and can inform the design

of dissipative biomaterials to optimize therapies targeting ECMs.

RESULTS

A chemo-mechanical model for invadopodia growth that integrates mechanical force balance with mechano-sensitive signaling pathways

Invadopodia are actin-rich protrusions that extend from the cell membrane into the surrounding ECMs (Figure 1A). Polymerization of actin monomers into filaments (F-actins) generates the protrusive force necessary for the invadopodium to grow. As the F-actins assemble, myosin contractility pulls them toward the cell center, generating actin retrograde flow; this actin flow can be slowed by the formation of adhesions that bind the F-actin to the ECM (Chan and Odde, 2008). Considering an invadopodium of length $R(t)$, its extension rate can be expressed as the difference between polymerization speed V_p and retrograde flow velocity V_r, i.e., $dR/dt = V_p - V_r$.

Polymerization-associated extension

To understand the interplay of matrix, polymerization, myosin, and adhesions, we examined the forces acting on the F-actins.

Myosin motors engaged with F-actins generate a pulling force F_m, related to retrograde flow V_r through Hill's relation (Hill, 1974), $F_m = F_M(1 - V_r/V_0)$; a high level of retrograde flow reduces the pulling force. Here, V_0 is the maximum retrograde flow velocity and F_M represents the maximum force generated by bound myosin motors. The stochastic binding and unbinding of adhesion molecules that connect F-actins with matrices provide a frictional resistance force, $F_a = \zeta_r V_r$, where ζ_r is an adhesive frictional coefficient. Since the cytoskeleton exhibits viscoelastic behavior (Alcaraz et al., 2003; Cartagena and Raman, 2014; Gong et al., 2019), we describe it with a Kelvin-Voigt model. Thus, as invadopodia extend, the cortical cytoskeleton provides a resistance force, $F_c = A(E_c\varepsilon_r + \eta_c\dot{\varepsilon}_r)$. Here A, E_c, and η_c are the invadopodium cross-sectional area, cytoskeleton elastic modulus, and viscous modulus, respectively; $\varepsilon_r = R/R_0$ denotes the cortical cytoskeleton strain, where R_0 is the initial length of the F-actins. Since the sum of all the forces on the F-actin bundle should vanish, we have: $F_m - F_a + F_c + F_e = 0$, which can also be expressed as:

$$\underbrace{F_M\left(1 - \frac{V_p - dR/dt}{V_0}\right)}_{\text{Myosin force}} - \underbrace{\zeta_r\left(V_p - \frac{dR}{dt}\right)}_{\text{Adhesion force}} + \underbrace{AE_c\frac{R(t)}{R_0} + A\eta_c\frac{dR}{R_0 dt}}_{\text{Cytoskeleton force}}$$

$$+ \underbrace{F_e}_{\text{ECM force}} = 0, \qquad (1)$$

where F_e is the ECM force that resists invadopodium extension, which we consider next.

Plastic deformation of ECMs
To calculate the ECM force F_e, we consider the stress-strain relation of our IPN hydrogels used for 3D cell culture; these IPN hydrogels are known to display irreversible deformation for creep-recovery tests, indicating the presence of mechanical plasticity (Wisdom et al., 2018). To model the mechanical response of IPN gels, we introduce a viscoplastic model that includes elastic, viscous, and plastic components in series (Figure 1C). For the plastic component, a Bingham plastic element (Bower, 2010; Liu et al., 2016) is placed in parallel with a spring and dashpot. The plastic strain changes only if the stress exceeds the yield stress σ_y, such that the plastic strain rate $d\varepsilon_p/dt$ is given by:

$$\frac{d\varepsilon_p}{dt} = \begin{cases} 0, & \sigma - E_2\varepsilon_p \leq \sigma_y \\ \frac{1}{\eta_2}(\sigma - \sigma_y - E_2\varepsilon_p), & \sigma - E_2\varepsilon_p > \sigma_y \end{cases}. \qquad (2)$$

Here $\sigma = F_e/A$ is the ECM stress, and E_2 and η_2 are the elastic and viscous moduli for the plastic component (Figure 1C). The total strain ε is expressed as the sum of the elastic strain ε_e, viscous strain ε_v, and plastic strain ε_p, with the strain rate written as:

$$\frac{d\varepsilon}{dt} = \frac{d\sigma}{E_0 dt} + \frac{1}{\eta_1}\left[\left(1 + \frac{E_1}{E_0}\right)\sigma - E_1(\varepsilon - \varepsilon_p)\right] + \frac{d\varepsilon_p}{dt}. \qquad (3)$$

The first term is the elastic strain rate $d\varepsilon_e/dt$, where E_0 is the initial elastic modulus; the second term represents the viscous strain rate $d\varepsilon_v/dt$ using a Kelvin-Voigt model, where E_1 and η_1

are elastic and viscous moduli for the viscous component. Our model proposed here can quantitatively fit the experimental data from creep-recovery tests (Figures 1D, S1A–S1F, and S2; see STAR Methods).

Mechano-sensitive recruitment of myosin
The dynamics of myosin recruitment to F-actins are governed by mechano-sensitive signaling pathways that originate at the adhesions; Rho GTPases increase myosin II ATPase activity through their effector Rho-associated kinase (ROCK) (Huveneers and Danen, 2009; Jerrell and Parekh, 2016; Shenoy et al., 2016). Conversely, Rac1 kinases (other members of the Rho family GTPases) inhibit Rho-GTP formation and reduce myosin activity (Clark et al., 2007; Nimnual et al., 2003). Therefore, tensile adhesion force, F_a, can increase myosin activity through the Rho-ROCK signaling pathway, while a high protrusion rate dR/dt reduces myosin activity via the Rac1 pathway (Figure 1B). By assuming that the myosin recruitment rate depends linearly on both adhesion force and protrusion rate (characterized by non-dimensional parameters α_0 and β_0, respectively), we can write the recruitment rate as $k_{on}^* = k_{on}^0 + \frac{\alpha_0 k_{on}^0 F_a}{f_b} - \frac{\beta_0}{R_0}\frac{dR}{dt}$; here k_{on}^0 and f_b represent the initial recruitment rate and characteristic force per myosin, respectively. The second term in the expression for k_{on}^* denotes an increase in the recruitment rate with the adhesion force, F_a, due to the Rho-ROCK pathway, and the third term denotes the inhibitory effect of Rac1 on myosin dynamics, which is related to protrusion rate, dR/dt. The rate of change in the bound myosin number can be written as (Huxley, 1957; McEvoy et al., 2019):

$$\frac{dm_b}{dt} = k_{on}^*(m_0 - m_b) - k_{off}m_b + \xi_m(t), \qquad (4)$$

where k_{off} is the dissociation rate of myosin from F-actins, and $m_0 - m_b$ and m_b indicate the unbound and bound number of myosin, respectively. We account for random fluctuations in the myosin recruitment dynamics by adding a Gaussian noise term, $\xi_m(t)$. Note that the force generated by bound myosin, i.e., $F_M = m_b f_b$, is the maximum myosin pulling force F_M (stated in Equation 1). By incorporating myosin recruitment dynamics into the mechanical force balance, we can simulate invadopodia extension dynamics (Figures 2A–2D). The values of parameters in our model are given in Table S1, and a detailed model description can be found in STAR Methods.

Invadopodia oscillations are governed by a competition between polymerization-associated extension and signaling-associated myosin recruitment dynamics
By solving Equations 1, 2, 3, and 4 (Figure S3; see STAR Methods), our chemo-mechanical model can simulate the oscillatory behavior (i.e., protrusion and retraction cycles) of invadopodia (Figure 2A). To study how the interplay between critical intracellular processes and matrix mechanics control oscillations, we compute the time evolution of retrograde flow, myosin pulling force, adhesion force, and ECM force (Figures 2B–2D). We can outline five stages of the protrusion and retraction cycle (Figure 2E):
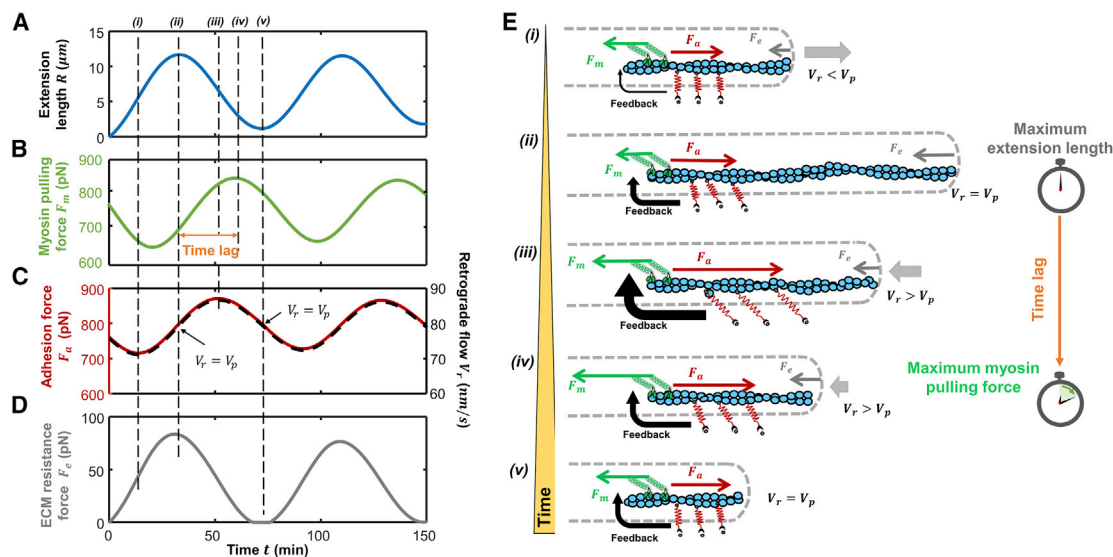
Figure 2. Mechanisms responsible for invadopodia oscillations
(A–D) Simulated invadopodia extension length R (A), myosin pulling force F_m (B), adhesion force F_a (red line) (C), retrograde flow (dashed line) (C), and matrix resistance force F_e (D) plotted as a function of time. There is a time lag between the peak extension length and the peak myosin pulling force.
(E) Schematic showing interplay of intracellular processes in the different oscillation stages.

(1) The invadopodium protrudes when the polymerization speed exceeds the retrograde flow velocity. As the ECM becomes increasingly deformed by the protrusion, its resistance force F_e increases. There is an associated increase in the retrograde flow velocity and a slowing of the extension rate (via Equation 1).

(2) When the retrograde flow velocity and the polymerization speed are equal, the invadopodium can no longer extend and attains a maximum length.

(3) The retrograde flow velocity continues to increase to a maximum value, exceeding the polymerization speed, and the invadopodium starts retracting. Meanwhile, there is a high (instantaneous) adhesion force F_a that triggers stress-mediated feedback signaling for myosin recruitment.

(4) The strong signaling feedback increases myosin recruitment (via Equation 4), leading to a maximum myosin force. The time delay associated with the signaling feedback and myosin recruitment leads to the phase difference between the myosin dynamics and the extension processes (Figures 2A–2D).

(5) The retrograde flow continues to decrease due to the reduction in myosin and matrix forces, and again equals the polymerization speed, stalling the invadopodium retraction. The next protrusion cycle begins when the decreasing retrograde flow velocity is lower than the polymerization speed.

In short, two key processes regulate the invadopodia oscillations: polymerization-associated extension dynamics and myosin recruitment dynamics. Myosin force continues to increase when invadopodia reach their maximum length, and protrusions begin to retract in response to high contractile

forces; when myosin force decreases and polymerization dominates, invadopodia start to grow again. The back-and-forth interaction between the two dynamics regulates the oscillations.

Matrix plastic strain accumulates by cyclic ratcheting during invadopodia oscillation

Next, we studied how strains evolve in viscoplastic ECMs during each of the oscillation stages (1–5) discussed in the previous section. In stage 1, the matrix is in contact with the invadopodium but has not yet been deformed. As the ECM becomes deformed and increasingly resists the extension of the invadopodium, the extension velocity begins to decrease. When the extension velocity reduces to zero, the invadopodium reaches a maximal extension (stage 2), and a peak force is achieved (Figures 3A–3D); the invadopodium begins to retract. In stages 3 and 4, its tip separates from the ECM, and the ECM force reduces to zero (identified by orange markers in Figures 3A and 3B). If protrusive forces are large enough to cause plastic yielding in the ECM, a gap forms between the retracted invadopodium tip and the matrix. When retraction velocity becomes zero, the invadopodium retracts to its minimal length and prepares for the next cycle (stage 5). To experimentally validate our model, we utilized our recently developed viscoplastic IPN hydrogels (Wisdom and Chaudhuri, 2017; Wisdom et al., 2018), which consist of rBM and alginate (see STAR Methods). We encapsulated highly invasive MDA-MB-231 cells transfected with red fluorescent protein (RFP)-LifeAct within the viscoplastic IPN hydrogels and then tracked invadopodia dynamics using time-lapse confocal microscopy. We identified the individual stages by which invadopodia (white dashed line in Figure 3E) deform the matrix (yellow dashed line in Figure 3E),
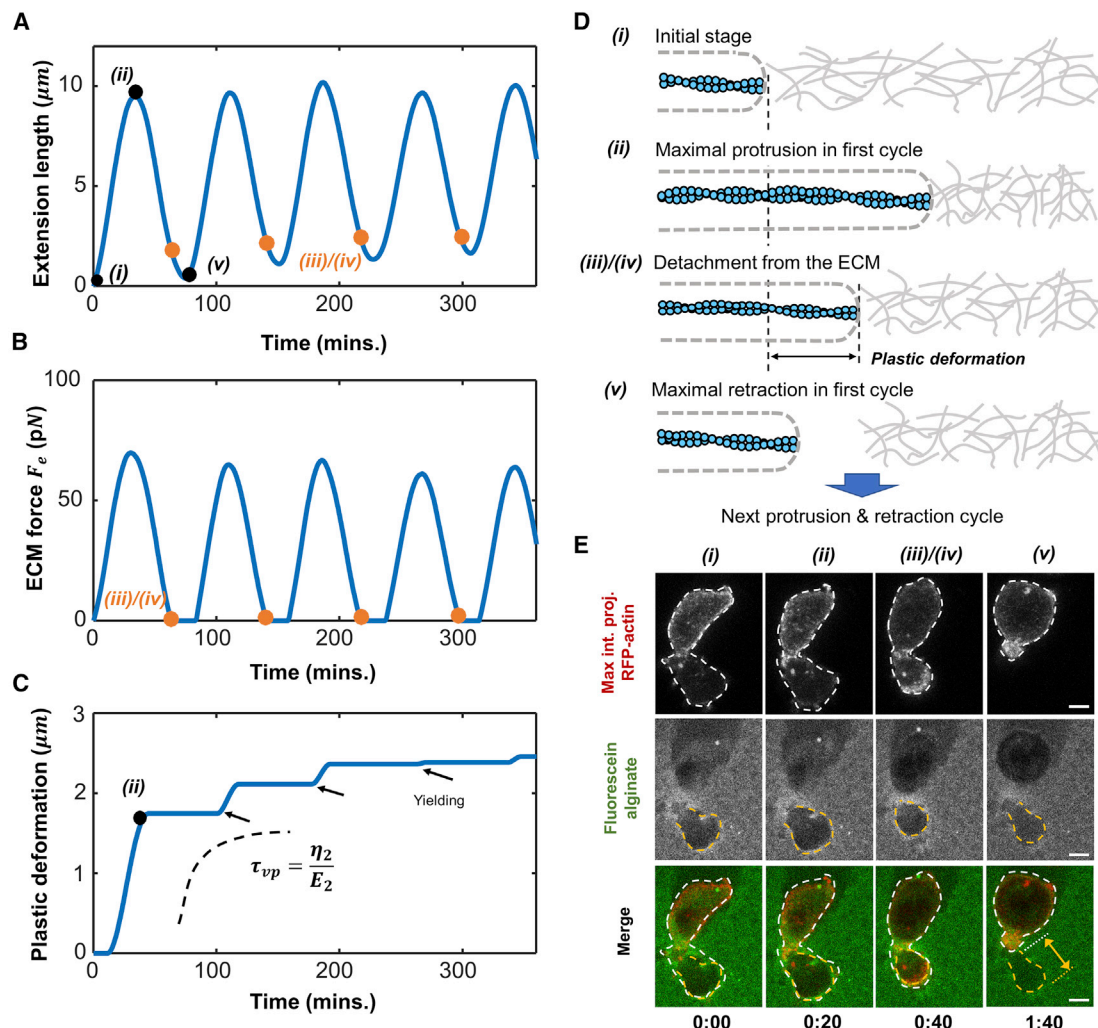
Figure 3. Simulation shows oscillatory extension of invadopodia in viscoplastic matrices

(A–C) Simulated invadopodia extension length (A), ECM force (B), and plastic deformation (C) of ECM plotted as a function of time.

(D) Schematic depicting the behavior of viscoplastic ECM in different stages of oscillation, marked in (A)–(C).

(E) Confocal fluorescence time-lapse images of MDA-MB-231 cells showing similar stages of invasive protrusion as predicted by the model (RFP-labeled actin, red; fluorescein-labeled matrices, green). The plastic deformation of the ECM (yellow line in the merged panel) remains after the retraction of the invadopodium. Scale bars, 5 μm. Timescale, h:min.

in line with our model predictions. Importantly, we also identified a large gap (arrowhead line in Figure 3E) between ECM (green) and the cell (red) following invadopodium retraction, confirming predictions for the presence of plastic deformation in viscoplastic ECMs.

As the oscillatory extension of the invadopodium continues across multiple cycles, the viscoplastic matrix is cyclically deformed. Over the repeated cycles, matrix dissipation softens the ECM, leading to an accumulation of plastic deformation (Figure 3C), also referred to as cyclic ratcheting. Over time, the ECM becomes more difficult for the invadopodium to produce additional plastic deformation due to plastic strain-hardening, leading to a steady state with no further increase in plastic strain (Figure 3C). The time at which the plastic deformation saturates is governed by the ECM's viscoplastic timescale

$\tau_{vp} = \eta_2/E_2$ (Figures S4A and S4B). Interestingly, the saturation of plastic deformation after cyclic loading can be verified by repeated creep-recovery tests on IPN hydrogels, from which a viscoplastic timescale of $\tau_{vp} \sim 10^3$s can be identified (Figures S1G and S1H). Our viscoplastic solid model proposed here can also quantitatively fit the experimental data from the repeated creep-recovery tests (Figures S1G–S1I and S2; see STAR Methods).

Viscoplasticity facilitates invadopodia oscillations by softening ECM over repeated cycles

Next, we investigated how ECM plasticity affects invadopodia dynamics. We utilized a series of IPN hydrogels (Wisdom et al., 2018), in which mechanical plasticity can be tuned independent of elasticity and ligand density to create IPNs of high
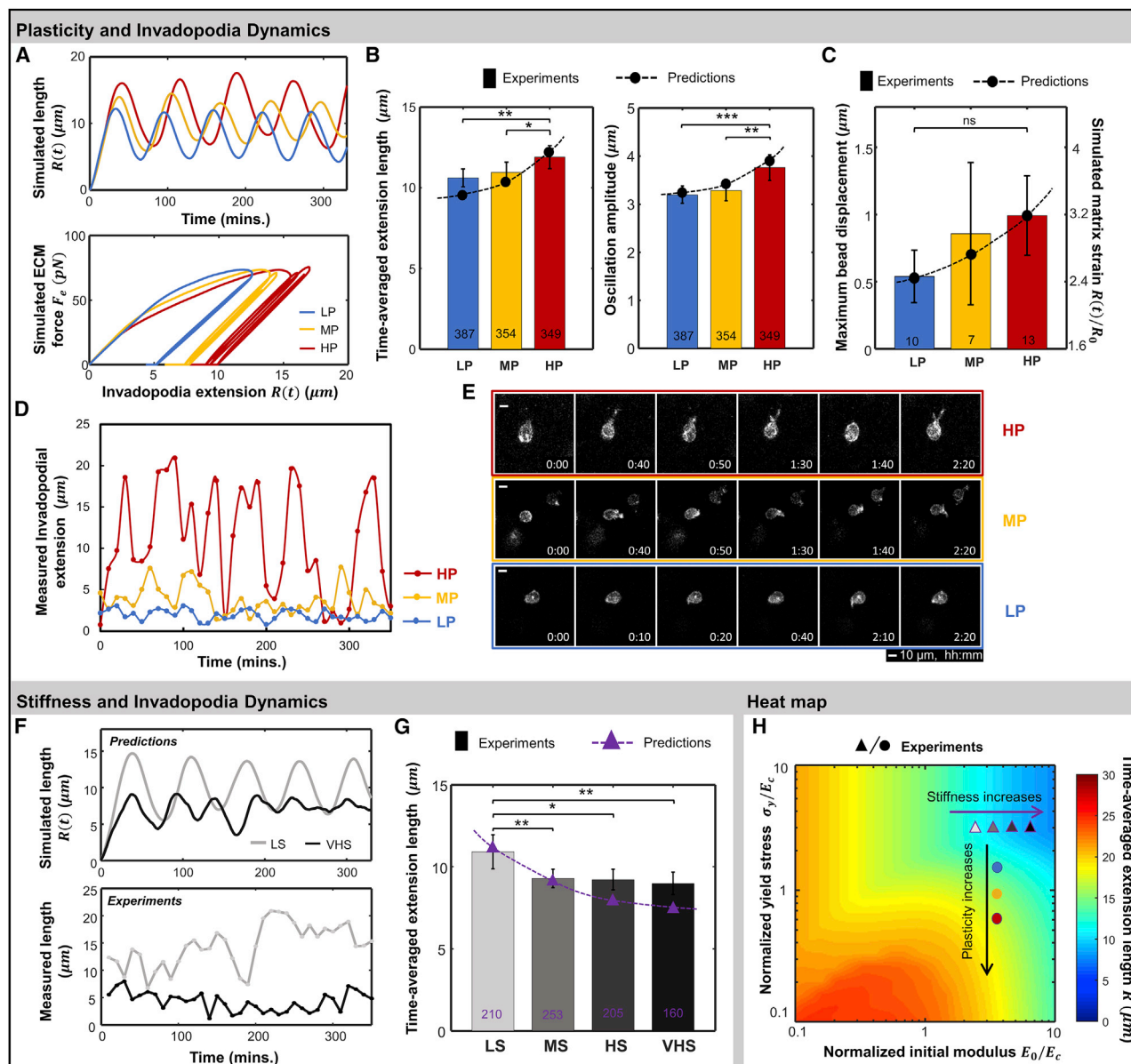
Figure 4. Model captures the impact of matrix plasticity and stiffness on invadopodia dynamics

(A) (Top panel) Simulated invadopodia extension versus time with respect to different levels of matrix plasticity, i.e., LP (low plasticity; blue line), MP (medium plasticity; yellow line), and HP (high plasticity; red line). (Bottom panel) Force exerted on the ECM by invadopodia plotted as a function of extension length for different plasticity levels.

(B) (Left panel) Time-averaged invadopodia extension length for different plasticity levels. (Right panel) Oscillation amplitude with respect to different plasticity levels. Dashed lines with circles denote simulation results. Data were obtained from three to five experimental replicates.

(C) The maximum bead displacement around cells plotted with different matrix plasticity levels (data extracted from Wisdom et al., 2018). The dashed line with circles denotes simulated matrix strain (right y axis).

(D) Invadopodia extension measured with a 10-min time interval for one representative cell each in LP (blue), MP (yellow), and HP (red) ECMs.

(E) Fluorescence images of representative RFP-LifeAct-transfected MDA-MB-231 cells in LP, MP, and HP matrices using time-lapse microscopy. Scale bars, 10 μm.

(F) (Top panel) Simulated length and (bottom panel) experimentally measured invadopodia length for a representative cell in ECMs with low stiffness (light gray) and very high stiffness (black).

(G) Time-averaged invadopodia extension length with respect to matrix stiffness (low stiffness 0.4 kPa [LS], medium stiffness 1.5 kPa [MS], high stiffness 4.4 kPa [HS], and very high stiffness 9.3 kPa [VHS]). Dashed line with triangles denotes simulation results.

(H) Heatmap showing how initial modulus and yield stress (normalized by cytoskeleton elastic modulus) regulate time-averaged extension length $\overline{R}$ of invadopodia. The circles/triangles represent the experimental results from three to four experimental replicates. The circles from top to

(legend continued on next page)

plasticity (HP), medium plasticity (MP), and low plasticity (LP) (see STAR Methods). In the viscoplastic model, the yield stress σ_y was modified to account for different levels of plasticity exhibited by IPN hydrogels (Figures S1B–S1E). Our subsequent simulations revealed that HP facilitates oscillatory growth of invadopodia (Figures 4A and 4B); at lower levels of yield stress (i.e., high levels of plasticity), the ECM can be more readily plastically deformed, leading to a larger gap (~10 μm) between the invadopodium tip and the ECM following retraction (Figure 4A). Furthermore, our simulations predict that invadopodia in HP matrices attain larger oscillation amplitudes compared to those in MP and LP matrices (circles in Figure 4B).

To verify our predictions experimentally, we encapsulated MDA-MB-231 cells within IPN hydrogels of different plasticity levels and measured time-dependent invadopodia extension lengths (Figures 4D and 4E). By performing a high-throughput analysis of invadopodia dynamics (Figure S5; see STAR Methods), we observed that invadopodia indeed exhibit longer time-averaged lengths (~10 μm) and larger oscillation amplitudes in HP matrices compared to MP and LP cases (Figures 4B and 4D; Videos S1, S2, and S3). Importantly, the experimentally measured lengths and oscillation amplitudes can be quantitatively predicted by our model (Figure 4B). Moreover, HT-1080 cells were also found to have oscillatory invadopodia and become more protrusive (with lower circularities) in HP matrices (Figures S6A and S6B), in line with our model predictions. By analyzing the displacements of fluorescent beads encapsulated in the matrix, we indeed found that the maximum matrix displacements are larger in HP matrices than in MP and LP matrices, in line with the simulated matrix strain (Figure 4C). These findings validate our predictions that high matrix plasticity facilitates oscillatory growth of invadopodia through large, permanent deformations.

To summarize the effects of matrix plasticity, we developed a heatmap of the time-averaged invadopodia length as a function of normalized initial ECM modulus and yield stress. The heatmap shows that invadopodia grow longer as the ECM yield stress decreases (black arrows in Figure 4H), with the experimentally observed dependence on plasticity marked by circles. In addition to the influence of plasticity, the dependence of invadopodia length on matrix stiffness can be predicted using our simulated heatmap (Figure 4H). The heatmap indicates that the invadopodia extension length decreases as elastic modulus increases (purple arrow in Figure 4H) due to the larger resistance encountered by invadopodia in stiffer ECMs. Interestingly, by utilizing the same type of IPN hydrogels of varying elastic stiffnesses (low stiffness [LS], medium stiffness [MS], high stiffness [HS], and very high stiffness [VHS]; see STAR Methods) (Chang et al., 2020), we found that cells have shorter invadopodia lengths in stiffer ECMs (Figures 4F and 4G). By varying the model parameter associated with stiffness (i.e., elastic modulus E_0), we can quantitatively fit the model to the experimental data. The excellent

agreement between our predictions and experimental results lends strong support for the fidelity of our model.

## Model predicts the influence of pharmacological treatments on invadopodia dynamics

To further validate our model, we simulated the effects of inhibiting key components (i.e., integrin, myosin, and the Rho-ROCK pathway) on invadopodia dynamics and performed pharmacological treatments to test our predictions. We first assessed the influence of integrin inhibition by decreasing the adhesive viscosity ζ_r in our model (Figure S7A). We found that when adhesions are impaired, retrograde flow velocity increases due to a lowering of resisting adhesion force, which subsequently reduces the extension rate and the time-averaged length. To experimentally verify our predictions, we treated MDA-MB-231 cells encapsulated in HP matrices with β1 integrin blocking antibody. In agreement with our model, we observed the reduced time-averaged invadopodia length (Figure 5A). Next, to assess the influence of contractility on the invadopodia growth, we decreased myosin-associated parameters, including feedback parameters α, β, and initial contractile force F_{M0} (Figures S7A and S7B). These alterations were predicted to reduce myosin contractility, stall retrograde flow, and ultimately increase invadopodia extension length. In our experiments, we inhibited the Rho-ROCK signaling pathway or myosin contractility by treating cells with Y27632 or blebbistatin, respectively. Compared to the control cells in HP matrices, invadopodia grew much longer after either treatment, again in line with model predictions (Figures 5A and 5B).

In addition to studying how the pharmacological treatments influence invadopodia length, we investigated how these treatments affect invadopodia oscillations. We considered the amplitude ratio r_a (i.e., the ratio between the oscillation amplitude and the time-averaged length, Figure S8A) as an index to quantify the variation of length relative to its mean value; a higher amplitude ratio indicates more oscillatory invadopodia (Figure S8B). We found that all of the treatments shift the distribution of the amplitude ratio toward lower amplitude ratios and significantly reduce the mean values (Figures 5C and 5D); the high oscillation fraction ($r_a > 0.5$) of invadopodia is reduced, while the low oscillation fraction ($r_a < 0.25$) is increased after treatments (Figure 5E). Taken together, these results (Figures 5C–5E) indicate that the pharmacological treatments inhibit invadopodia oscillations. The inhibition effects of different treatments also agree with our model predictions, as we found that reducing the model parameters associated with a given treatment can lead to non-oscillatory or monotonically growing protrusion (Figures S7E–S7G). The combined experimental and simulated results demonstrate that different intracellular processes, including adhesion dynamics, the Rho-ROCK pathway, and myosin recruitment, act cooperatively to control invadopodia oscillations; disrupting any of the key processes can cause invadopodia to become less oscillatory.

bottom correspond to invadopodia in LP, MP, and HP ECMs, while the triangles from left to right correspond to invadopodia in LS, MS, HS, and VHS ECMs, respectively.

For (B), (C), and (G), bar plots display the number of cells analyzed per condition, and error bars indicate 95% confidence intervals (*p < 0.05, **p < 0.01, ***p < 0.001, ANOVA with Benjamini-Hochberg procedure).
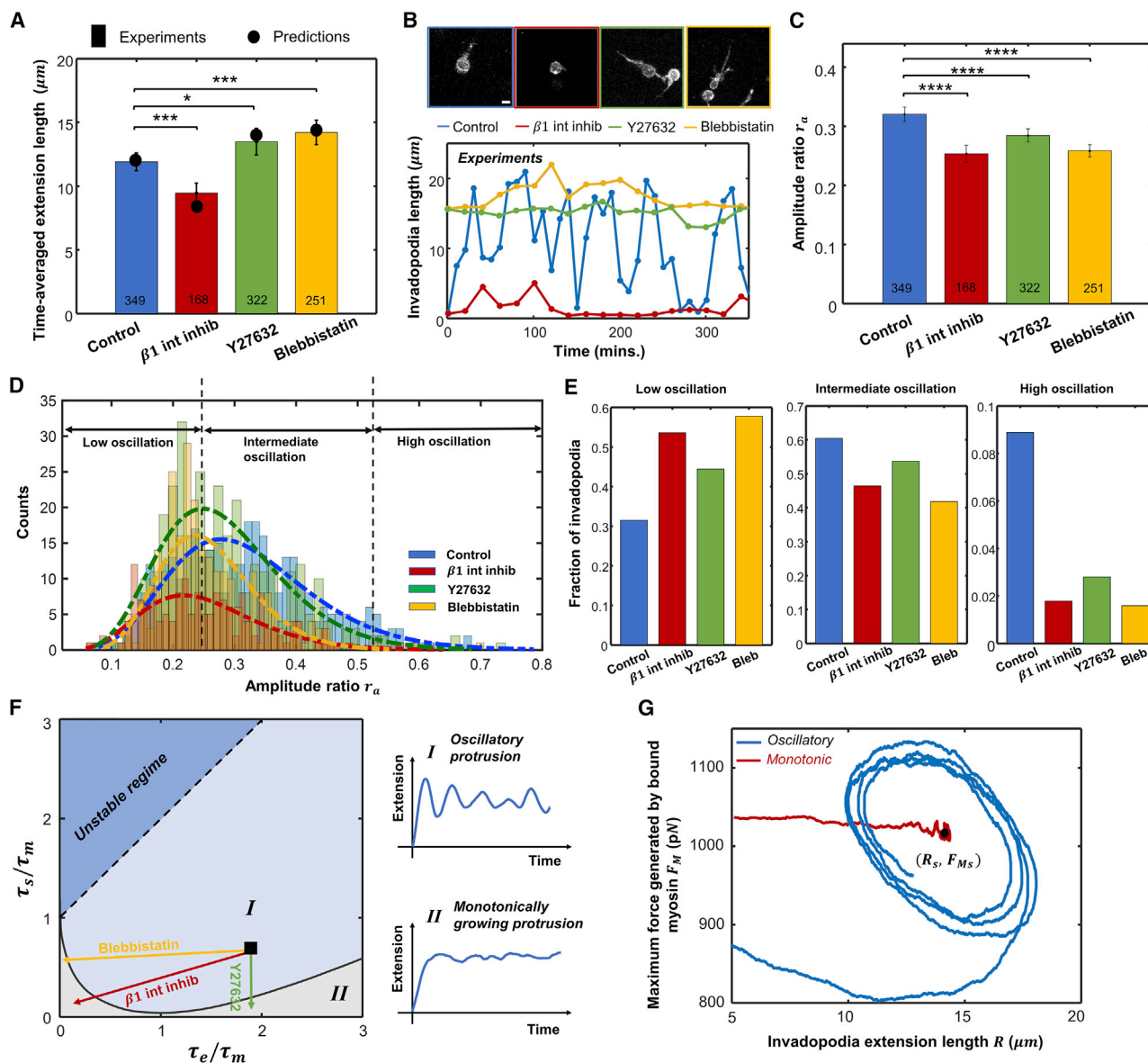
Figure 5. Model predicts changes in invadopodia dynamics upon inhibition of β1 integrin, the Rho-ROCK pathway, and myosin activity

(A) The time-averaged extension length of invadopodia for control (blue) and different inhibitor treatments. Integrin, the Rho-ROCK pathway, and myosin activity are inhibited by β1 integrin inhibitor (red), Y27632 (green), and blebbistatin (yellow), respectively. Circles denote simulation results.

(B) (Top panel) Representative RFP-LifeAct fluorescence images show cells for control and different treatments. Scale bar, 10 μm. (Bottom panel) Representative curves showing the evolution of protrusion length for experiments with different treatments.

(C) The amplitude ratio r_a plotted for control and different treatments.

(D) Distribution of amplitude ratios for control and different treatments. The dashed lines represent fitted density functions of log-normal distribution. Three regimes indicating low ($r_a < 0.25$), intermediate ($0.25 < r_a < 0.5$), and high ($r_a > 0.5$) levels of oscillation are labeled.

(E) Fraction of invadopodia with (left panel) low level, (middle panel) intermediate level, and (right panel) high level of oscillation for control and different treatments.

(F) Phase diagram showing two types of protrusion patterns: oscillatory protrusions (regime I) and monotonically growing protrusions (regime II), based on extension-associated viscous timescale τ_e and signaling-associated myosin recruitment timescale τ_s normalized by the intrinsic myosin recruitment timescale τ_m. The arrows indicate the influence of β1 integrin blocking antibody (red), blebbistatin (yellow), and Y27632 (green) treatments on the protrusion patterns.

(G) The phase space of maximum force generated by bound myosin F_M and invadopodia extension length R for oscillatory (blue line) and monotonical (red line) behavior. The black circled marker represents the steady-state point (R_s, F_{Ms}).

In (A) and (C), a bar plot displays the number of cells analyzed per condition, taken from three to five biological replicate experiments. Error bars indicate 95% confidence intervals (*p < 0.05, ***p < 0.001, ****p < 0.0001, ANOVA with Benjamini-Hochberg procedure).

Timescales of extension-associated viscosity and signaling-associated myosin recruitment determine the distinct patterns of invadopodia behavior

To understand why the pharmacological treatments inhibit oscillation, we performed a linear stability analysis on the governing equations for invadopodia dynamics (see STAR methods). This analysis yields the characteristic timescales governing the two key oscillation-regulating processes, i.e., polymerization-associated extension and myosin recruitment dynamics. The extension dynamics are characterized by an extension-associated viscous timescale: $\tau_e = \zeta_r / k_t + \eta_c / E_t + F_{Ms}/(k_t V_0)$. This viscous timescale τ_e has three terms representing three different viscous processes; ζ_r / k_t characterizes the frictional interaction between adhesions and ECMs, η_c / E_t characterizes cytoskeleton relaxation, and $F_{Ms}/(k_t V_0)$ characterizes the effective myosin viscosity (associated with Hill's force-velocity relation). Here, k_t and E_t represent the effective stiffness and modulus sensed by invadopodia, respectively, while $F_{Ms} = F_{M0} + \alpha \zeta_r V_p$ is the maximum force generated by bound myosin at the steady state. Myosin recruitment is regulated by both the intrinsic and the signaling-associated myosin recruitment, which can be characterized by the timescales $\tau_m = 1/k_{off}$ and $\tau_s = (\alpha + \beta) \zeta_r / k_t (1 - V_p / V_0)$, respectively. In the expression for τ_s, the terms α and β describe the influence of Rho-ROCK and Rac1 signaling on myosin recruitment, respectively.

The linear stability analysis also allows for the generation of a phase diagram that shows distinct phases of dynamic behavior, i.e., an oscillatory or monotonically growing (non-oscillatory) pattern (Figures 5F and 5G). We found that invadopodia spontaneously oscillate when timescales for extension and signaling-associated myosin recruitment are comparable, i.e., $\tau_e \approx \tau_s$ (regime I in Figure 5F). Note that the amplitudes of the spontaneous oscillation should, in theory, decrease gradually over time; this is not the case as random fluctuations in myosin recruitment (via $\xi_m(t)$ in Equation 4) cause deviations in the myosin force from its steady state, initiating excursions in the phase space of extension length and myosin force (Figures 5G and S9A–S9C). Eventually, the random fluctuations sustain an oscillation with a random amplitude, but a fixed time period given by $\sim 2\pi \sqrt{\tau_m \tau_e}$ (refer to STAR Methods). In regime II, the invadopodium has a low signaling-associated myosin recruitment timescale τ_s (i.e., $\tau_s \ll \tau_e$), corresponding to weak signaling feedback; the extension dynamics dominate, leading to non-oscillatory behavior (Figures S8D and S8E). However, these two protrusion patterns are difficult to differentiate in experimental measurements, as experimental noises, associated with random fluctuations in myosin dynamics or noise from microenvironments, also leads to time-dependent variations in length. Yet, the behavior of invadopodia after treatment (with low amplitude ratios) is more closely representative of monotonic growth (Figures 5B–5E). As the timescales that characterize different processes are modified by different pharmacological treatments (arrows in Figure 5F), invadopodia dynamics can fall into regime II (i.e., exhibiting non-oscillatory patterns). Thus, the phase diagram can also be used to predict the influence of different treatments.

DISCUSSION

In this study, we propose a chemo-mechanical model to describe how cells exploit invadopodia to dynamically probe the mechanical plasticity of ECMs in an oscillatory manner. Invadopodia oscillation requires the cooperation of multiple intracellular processes, including myosin contractility, adhesion dynamics, actin polymerization, and mechano-sensitive signaling pathways. During an oscillation, invadopodia can sense time-dependent ECM properties (i.e., viscoelasticity or viscoplasticity) by gauging the time dependence of resistance forces from the matrix. Combining our model with experiments, we show that high ECM plasticity facilitates oscillatory growth of invadopodia. Furthermore, we predict and experimentally validate the influence of pharmacological treatments on invadopodia dynamics, specifically targeting myosin activity, adhesions, and the Rho-ROCK signaling pathway.

The effect of dissipative matrix properties on cell motility has become an active area of research, as most ECMs are found to be viscoelastic and viscoplastic (Chaudhuri et al., 2020). To study the influence of viscoelasticity, different biomaterials with tunable viscoelasticity, such as alginate hydrogels (Chaudhuri et al., 2015, 2016), crosslinked polyacrylamide gels (Cameron et al., 2011; Charrier et al., 2018; Mandal et al., 2020), and hyaluronic-acid-based hydrogels (Loebel et al., 2019), have been developed. Studies have demonstrated that viscosity can regulate cell spreading and differentiation (Chaudhuri et al., 2015, 2016). To physically understand the influence of viscoelasticity, the motor clutch model has been adapted to show that viscosity serves to stiffen soft substrates on a timescale faster than the bond dissociation rate, which enhances cell-matrix adhesion and cell spreading (Gong et al., 2018). In addition to viscosity, matrix plasticity can also regulate cell spreading on 2D substrates. A recent study has shown that substrate plasticity controls cell spreading through a biphasic relationship that depends on cell contractility (Grolman et al., 2020). Nevertheless, in our study, we have gone beyond these previous studies in 2D systems. We have developed a chemo-mechanical model to study the role of matrix plasticity in cell mechano-transduction in 3D confining environments relevant in disease models, and our predictions have been validated using the recently developed viscoplastic IPN hydrogels (Wisdom and Chaudhuri, 2017) in 3D environments.

ECM plasticity, which endows matrices with an intrinsic ability to possess long-term memory, suggests that the matrix can serve as a mechanical storage device that is "written on" or "read" by cells (DuFort et al., 2011). Oscillating invadopodia cyclically deform viscoplastic ECMs, leading to cyclic ratcheting behavior. In this process, permanent deformation (information written on the ECM by invadopodia) gradually accumulates and gets saturated (Figures 3C and 4A). In turn, large plastic deformation in HP ECMs (which is read by cells) presents invadopodia with less resistance and thereby facilitates invadopodia extension to longer lengths (Figure 4A). The saturation time for plastic deformation is governed by the ECM's viscoplastic timescale $\tau_{vp} = \eta_2/E_2 \sim 10^3 s$, indicating that, after a long time ($t \gg \tau_{vp}$), invadopodia can no longer plastically deform (or "write" permanent information) the ECM.

Although we developed a 1D model, our framework describes invadopodia dynamics in 3D confining environments, accounting for how the ECM opposes invadopodia growth. Previous studies have shown that matrix rigidity can promote invadopodia activity (Alexander et al., 2008) and that an optimal rigidity can enhance invadopodia formation (Parekh et al., 2011). However, our model and experiments show that stiffer ECMs decrease invadopodia length due to significant resistance to extension-associated deformation (Figure 4H). A possible explanation for the difference in findings is the combined effect of protease-mediated ECM degradation and mechanical force generation in the previous studies (Alexander et al., 2008). In contrast, the 3D material system employed herein, composed primarily of alginate networks, is not degradable by cell-secreted enzymes (Wisdom et al., 2018). Hence, this new material system enables us to investigate mechano-sensing and force generation of invadopodia, independent of the proteolytic activity.

Our model can also be applied to other cell types and material systems. We found that HT-1080 cells also have oscillatory invadopodia and become more protrusive (with lower circularities) in HP matrices (Figure S6B). A recent study has also shown that, in collagen gels, invadopodia of MTLn3, MDA-MB-231, and Hs578T cells show oscillatory behaviors, although ECM degradation plays a role (Pourfarhangi et al., 2018). Taken together, these experiments on different cell types or material systems suggest the general applicability of our model. Meanwhile, recent studies have shown that ECM remodeling induced by cell protrusions also depends on actin nucleation in the cytoskeleton (Malandrino et al., 2019), heterogeneity in crosslink kinetics (Mak, 2020), and proteolytic activity of MT1-MMP (Ferrari et al., 2019). Future computational models may build upon our chemo-mechanical model by incorporating the features of the tumor microenvironment, including the proteolytic ECM degradation, growth factors, pH, nonlinear elasticity, matrix heterogeneity, and topographical cues, which are all known to regulate protrusion activity (Gould and Courtneidge, 2014; Malandrino et al., 2018).

Oscillations have not only been observed in invadopodia but also in other protrusions such as podosomes (van den Dries et al., 2013) and filopodia (Alieva et al., 2019; Marchenko et al., 2017), potentially suggesting the ubiquitous nature of oscillations in such nonlinear cellular systems. Although previous models (Marchenko et al., 2017; Nisenholz et al., 2016) have been developed to explain oscillatory behaviors, they typically neglect the role of mechano-sensitive signaling pathways; our study shows that the Rho-ROCK pathway and the mutually inhibitory roles of Rac1 and Rho are important biochemical processes closely associated with invadopodia oscillations (Figures 5A–5C). It is noteworthy that our model can also be extended to explain filopodia or lamellipodia dynamics in 2D environments. To model filopodial dynamics, we can remove the resisting force from the 3D matrices; in agreement with previous experimental findings (Alieva et al., 2019; Marchenko et al., 2017), we observed similar oscillatory behaviors (Figures S6C and S6D). Furthermore, the stochastic Monte Carlo simulation of adhesion molecules as force-dependent clutches (slip/catch bond) does not change the oscillation patterns; as the clutch dynamics only affect adhesion lifetimes on the order of several minutes (Bangasser and

Odde, 2013; Gong et al., 2018), it is negligible compared to the invadopodia oscillation period (~1 h).

Our analyses reveal that invadopodia oscillations are regulated by polymerization-associated extension and myosin recruitment dynamics, which are characterized by the extension-associated viscous timescale τ_e and signaling-associated myosin recruitment timescale τ_s, respectively. Invadopodia spontaneously oscillate when these two timescales are comparable (regime I in Figure 5F). The oscillation period can be estimated as $T \approx 2\pi\sqrt{\tau_m \tau_e} \sim 1\,h$, in line with the experimental observations. In addition to the oscillatory protrusion pattern, invadopodia can exhibit monotonic behavior when the two timescales are not comparable (regime II in Figure 5F). Interestingly, we found that the pharmacological treatments that target myosin activity, adhesions, or Rho-ROCK pathways cause invadopodia to become less oscillatory (Figures 5B–5E); this agrees with our predictions, as the modified timescales by these treatments lead to non-oscillatory patterns. Furthermore, the less oscillatory protrusions might explain why cells with very long yet stagnant protrusions after blebbistatin and Y-27632 treatments migrate very little, as observed in the previous study (Wisdom et al., 2018). As the oscillatory invadopodia are observed prior to cell migration, it may suggest that the long and highly oscillatory invadopodia are required for cells in 3D environments to generate sufficient momentum for cells to squeeze through channels created by the protrusions.

In conclusion, the model proposed in this study describes how the interplay of multiple intracellular processes allows invadopodia protrusions to dynamically sense and respond to matrix plasticity. The fundamental understanding of invasion mechanics, as well as their dependence on ECM characteristics and intracellular mechano-sensitive signaling cascades, may help design dissipative biomaterials to modulate cancer cell motility and guide the development of cancer therapeutics targeting mechano-transduction of invadopodia in confining 3D environments.

STAR★METHODS

Detailed methods are provided in the online version of this paper and include the following:

Cell Reports
Article

CellPress
OPEN ACCESS

AUTHOR CONTRIBUTIONS

Z.G., K.M.W., O.C., and V.B.S. conceived and designed the experiments/simulations. K.M.W., J.C., and K.A. performed the experiments. Z.G. and K.M.W. analyzed the experimental data. Z.G., E.M., C.C.P., and V.B.S. conducted the modeling. Z.G., K.M.W., E.M., J.C., K.A., O.C., and V.B.S. wrote the paper.

DECLARATION OF INTERESTS

The authors declare no competing interests.

INCLUSION AND DIVERSITY

One or more of the authors of this paper self-identifies as an underrepresented ethnic minority in science. One or more of the authors of this paper received support from a program designed to increase minority representation in science.

SUPPORTING CITATIONS

The following references appear in the supplemental information: Anderson et al. (2008); Gong et al. (2016); He et al. (2016); Maiuri et al. (2015); Nisenholz et al. (2014); Yu et al. (2017).

REFERENCES

Alcaraz, J., Buscemi, L., Grabulosa, M., Trepat, X., Fabry, B., Farré, R., and Navajas, D. (2003). Microrheology of human lung epithelial cells measured by atomic force microscopy. Biophys. J. *84*, 2071–2079.

Alexander, N.R., Branch, K.M., Parekh, A., Clark, E.S., Iwueke, I.C., Guelcher, S.A., and Weaver, A.M. (2008). Extracellular matrix rigidity promotes invadopodia activity. Curr. Biol. *18*, 1295–1299.

Alieva, N.O., Efremov, A.K., Hu, S., Oh, D., Chen, Z., Natarajan, M., Ong, H.T., Jégou, A., Romet-Lemonne, G., Groves, J.T., et al. (2019). Myosin IIA and formin dependent mechanosensitivity of filopodia adhesion. Nat. Commun. *10*, 3593.

Alisafaei, F., Jokhun, D.S., Shivashankar, G., and Shenoy, V.B. (2019). Regulation of nuclear architecture, mechanics, and nucleocytoplasmic shuttling of epigenetic factors by cell geometric constraints. Proc. Natl. Acad. Sci. USA *116*, 13200–13209.

Anderson, T.W., Vaughan, A.N., and Cramer, L.P. (2008). Retrograde flow and myosin II activity within the leading cell edge deliver F-actin to the lamella to seed the formation of graded polarity actomyosin II filament bundles in migrating fibroblasts. Mol. Biol. Cell *19*, 5006–5018.

Artym, V.V., Zhang, Y., Seillier-Moiseiwitsch, F., Yamada, K.M., and Mueller, S.C. (2006). Dynamic interactions of cortactin and membrane type 1 matrix metalloproteinase at invadopodia: defining the stages of invadopodia formation and function. Cancer Res. *66*, 3034–3043.

Ban, E., Franklin, J.M., Nam, S., Smith, L.R., Wang, H., Wells, R.G., Chaudhuri, O., Liphardt, J.T., and Shenoy, V.B. (2018). Mechanisms of plastic deformation in collagen networks induced by cellular forces. Biophys. J. *114*, 450–461.

Bangasser, B.L., and Odde, D.J. (2013). Master equation-based analysis of a motor-clutch model for cell traction force. Cell. Mol. Bioeng. *6*, 449–459.

Bennett, M., Cantini, M., Reboud, J., Cooper, J.M., Roca-Cusachs, P., and Salmeron-Sanchez, M. (2018). Molecular clutch drives cell response to surface viscosity. Proc. Natl. Acad. Sci. USA *115*, 1192–1197.

Bower, A.F. (2010). Applied Mechanics of Solids (CRC Press).

Cameron, A.R., Frith, J.E., and Cooper-White, J.J. (2011). The influence of substrate creep on mesenchymal stem cell behaviour and phenotype. Biomaterials *32*, 5979–5993.

Cartagena, A., and Raman, A. (2014). Local viscoelastic properties of live cells investigated using dynamic and quasi-static atomic force microscopy methods. Biophys. J. *106*, 1033–1043.

Chan, C.E., and Odde, D.J. (2008). Traction dynamics of filopodia on compliant substrates. Science *322*, 1687–1691.

Chang, J., Pang, E.M., Adebowale, K., Wisdom, K.M., and Chaudhuri, O. (2020). Increased stiffness inhibits invadopodia formation and cell migration in 3D. Biophys. J. *119*, 726–736.

Charrier, E.E., Pogoda, K., Wells, R.G., and Janmey, P.A. (2018). Control of cell morphology and differentiation by substrates with independently tunable elasticity and viscous dissipation. Nat. Commun. *9*, 449.

Chaudhuri, O., Koshy, S.T., Branco da Cunha, C., Shin, J.-W., Verbeke, C.S., Allison, K.H., and Mooney, D.J. (2014). Extracellular matrix stiffness and composition jointly regulate the induction of malignant phenotypes in mammary epithelium. Nat. Mater. *13*, 970–978.

Chaudhuri, O., Gu, L., Darnell, M., Klumpers, D., Bencherif, S.A., Weaver, J.C., Huebsch, N., and Mooney, D.J. (2015). Substrate stress relaxation regulates cell spreading. Nat. Commun. *6*, 6364.

Chaudhuri, O., Gu, L., Klumpers, D., Darnell, M., Bencherif, S.A., Weaver, J.C., Huebsch, N., Lee, H.P., Lippens, E., Duda, G.N., and Mooney, D.J. (2016). Hydrogels with tunable stress relaxation regulate stem cell fate and activity. Nat. Mater. *15*, 326–334.

Chaudhuri, O., Cooper-White, J., Janmey, P.A., Mooney, D.J., and Shenoy, V.B. (2020). Effects of extracellular matrix viscoelasticity on cellular behaviour. Nature *584*, 535–546.

Clark, K., Langeslag, M., Figdor, C.G., and van Leeuwen, F.N. (2007). Myosin II and mechanotransduction: A balancing act. Trends Cell Biol. *17*, 178–186.

Discher, D.E., Janmey, P., and Wang, Y.L. (2005). Tissue cells feel and respond to the stiffness of their substrate. Science *310*, 1139–1143.

DuFort, C.C., Paszek, M.J., and Weaver, V.M. (2011). Balancing forces: Architectural control of mechanotransduction. Nat. Rev. Mol. Cell Biol. *12*, 308–319.

Elosegui-Artola, A., Bazellières, E., Allen, M.D., Andreu, I., Oria, R., Sunyer, R., Gomm, J.J., Marshall, J.F., Jones, J.L., Trepat, X., and Roca-Cusachs, P. (2014). Rigidity sensing and adaptation through regulation of integrin types. Nat. Mater. *13*, 631–637.

Enderling, H., Alexander, N.R., Clark, E.S., Branch, K.M., Estrada, L., Crooke, C., Jourquin, J., Lobdell, N., Zaman, M.H., Guelcher, S.A., et al. (2008). Dependence of invadopodia function on collagen fiber spacing and cross-linking: Computational modeling and experimental evidence. Biophys. J. *95*, 2203–2218.

Ferrari, R., Martin, G., Tagit, O., Guichard, A., Cambi, A., Voituriez, R., Vassilopoulos, S., and Chavrier, P. (2019). MT1-MMP directs force-producing proteolytic contacts that drive tumor cell invasion. Nat. Commun. *10*, 4886.

Génot, E., and Gligorijevic, B. (2014). Invadosomes in their natural habitat. Eur. J. Cell Biol. *93*, 367–379.

Gong, Z., You, R., Chang, R.C.-C., and Lin, Y. (2016). Viscoelastic response of neural cells governed by the deposition of amyloid-β peptides (Aβ). J. Appl. Phys. *119*, 214701.

Gong, Z., Szczesny, S.E., Caliari, S.R., Charrier, E.E., Chaudhuri, O., Cao, X., Lin, Y., Mauck, R.L., Janmey, P.A., Burdick, J.A., and Shenoy, V.B. (2018). Matching material and cellular timescales maximizes cell spreading on visco-elastic substrates. Proc. Natl. Acad. Sci. USA 115, E2686–E2695.

Gong, Z., Fang, C., You, R., Shao, X., Wei, X., Chang, R.C., and Lin, Y. (2019). Distinct relaxation timescales of neurites revealed by rate-dependent indentation, relaxation and micro-rheology tests. Soft Matter 15, 166–174.

Gould, C.M., and Courtneidge, S.A. (2014). Regulation of invadopodia by the tumor microenvironment. Cell Adhes. Migr. 8, 226–235.

Grolman, J.M., Weinand, P., and Mooney, D.J. (2020). Extracellular matrix plasticity as a driver of cell spreading. Proc. Natl. Acad. Sci. USA 117, 25999–26007.

He, B., Martin, A., and Wieschaus, E. (2016). Flow-dependent myosin recruitment during Drosophila cellularization requires zygotic dunk activity. Development 143, 2417–2430.

Hill, T.L. (1974). Theoretical formalism for the sliding filament model of contraction of striated muscle. Part I. Prog. Biophys. Mol. Biol. 28, 267–340.

Huveneers, S., and Danen, E.H. (2009). Adhesion signaling—Crosstalk between integrins, Src and Rho. J. Cell Sci. 122, 1059–1069.

Huxley, A.F. (1957). Muscle structure and theories of contraction. Prog. Biophys. Biophys. Chem. 7, 255–318.

Jerrell, R.J., and Parekh, A. (2016). Matrix rigidity differentially regulates invadopodia activity through ROCK1 and ROCK2. Biomaterials 84, 119–129.

Liu, A.S., Wang, H., Copeland, C.R., Chen, C.S., Shenoy, V.B., and Reich, D.H. (2016). Matrix viscoplasticity and its shielding by active mechanics in microtissue models: Experiments and mathematical modeling. Sci. Rep. 6, 33919.

Loebel, C., Mauck, R.L., and Burdick, J.A. (2019). Local nascent protein deposition and remodelling guide mesenchymal stromal cell mechanosensing and fate in three-dimensional hydrogels. Nat. Mater. 18, 883–891.

Maiuri, P., Rupprecht, J.F., Wieser, S., Ruprecht, V., Bénichou, O., Carpi, N., Coppey, M., De Beco, S., Gov, N., Heisenberg, C.P., et al. (2015). Actin flows mediate a universal coupling between cell speed and cell persistence. Cell 161, 374–386.

Mak, M. (2020). Impact of crosslink heterogeneity on extracellular matrix mechanics and remodeling. Comput. Struct. Biotechnol. J. 18, 3969–3976.

Malandrino, A., Mak, M., Kamm, R.D., and Moeendarbary, E. (2018). Complex mechanics of the heterogeneous extracellular matrix in cancer. Extreme Mech. Lett. 21, 25–34.

Malandrino, A., Trepat, X., Kamm, R.D., and Mak, M. (2019). Dynamic filopodial forces induce accumulation, damage, and plastic remodeling of 3D extracellular matrices. PLoS Comput. Biol. 15, e1006684.

Mandal, K., Gong, Z., Rylander, A., Shenoy, V.B., and Janmey, P.A. (2020). Opposite responses of normal hepatocytes and hepatocellular carcinoma cells to substrate viscoelasticity. Biomater. Sci. 8, 1316–1328.

Marchenko, O.O., Das, S., Yu, J., Novak, I.L., Rodionov, V.I., Efimova, N., Svitkina, T., Wolgemuth, C.W., and Loew, L.M. (2017). A minimal actomyosin-based model predicts the dynamics of filopodia on neuronal dendrites. Mol. Biol. Cell 28, 1021–1033.

McEvoy, E., Deshpande, V.S., and McGarry, P. (2019). Transient active force generation and stress fibre remodelling in cells under cyclic loading. Biomech. Model. Mechanobiol. 18, 921–937.

Murphy, D.A., and Courtneidge, S.A. (2011). The "ins" and "outs" of podosomes and invadopodia: characteristics, formation and function. Nat. Rev. Mol. Cell Biol. 12, 413–426.

Nam, S., Lee, J., Brownfield, D.G., and Chaudhuri, O. (2016). Viscoplasticity enables mechanical remodeling of matrix by cells. Biophys. J. 111, 2296–2308.

Nimnual, A.S., Taylor, L.J., and Bar-Sagi, D. (2003). Redox-dependent down-regulation of Rho by Rac. Nat. Cell Biol. 5, 236–241.

Nisenholz, N., Rajendran, K., Dang, Q., Chen, H., Kemkemer, R., Krishnan, R., and Zemel, A. (2014). Active mechanics and dynamics of cell spreading on elastic substrates. Soft Matter 10, 7234–7246.

Nisenholz, N., Paknikar, A., Köster, S., and Zemel, A. (2016). Contribution of myosin II activity to cell spreading dynamics. Soft Matter 12, 500–507.

Oser, M., Yamaguchi, H., Mader, C.C., Bravo-Cordero, J.J., Arias, M., Chen, X., Desmarais, V., van Rheenen, J., Koleske, A.J., and Condeelis, J. (2009). Cortactin regulates cofilin and N-WASp activities to control the stages of invadopodium assembly and maturation. J. Cell Biol. 186, 571–587.

Pakshir, P., Alizadehgiashi, M., Wong, B., Coelho, N.M., Chen, X., Gong, Z., Shenoy, V.B., McCulloch, C., and Hinz, B. (2019). Dynamic fibroblast contractions attract remote macrophages in fibrillar collagen matrix. Nat. Commun. 10, 1850.

Parekh, A., Ruppender, N.S., Branch, K.M., Sewell-Loftin, M.K., Lin, J., Boyer, P.D., Candiello, J.E., Merryman, W.D., Guelcher, S.A., and Weaver, A.M. (2011). Sensing and modulation of invadopodia across a wide range of rigidities. Biophys. J. 100, 573–582.

Pourfarhangi, K.E., Bergman, A., and Gligorijevic, B. (2018). ECM cross-linking regulates invadopodia dynamics. Biophys. J. 114, 1455–1466.

Prahl, L.S., Stanslaski, M.R., Vargas, P., Piel, M., and Odde, D.J. (2020). Predicting confined 1D cell migration from parameters calibrated to a 2D motor-clutch model. Biophys. J. 118, 1709–1720.

Rowley, J.A., Madlambayan, G., and Mooney, D.J. (1999). Alginate hydrogels as synthetic extracellular matrix materials. Biomaterials 20, 45–53.

Shenoy, V.B., Wang, H., and Wang, X. (2016). A chemo-mechanical free-energy-based approach to model durotaxis and extracellular stiffness-dependent contraction and polarization of cells. Interface Focus 6, 20150067.

Sibony-Benyamini, H., and Gil-Henn, H. (2012). Invadopodia: The leading force. Eur. J. Cell Biol. 91, 896–901.

Sunyer, R., Conte, V., Escribano, J., Elosegui-Artola, A., Labernadie, A., Valon, L., Navajas, D., García-Aznar, J.M., Muñoz, J.J., Roca-Cusachs, P., and Trepat, X. (2016). Collective cell durotaxis emerges from long-range intercellular force transmission. Science 353, 1157–1161.

Tolde, O., Rösel, D., Veselý, P., Folk, P., and Brábek, J. (2010). The structure of invadopodia in a complex 3D environment. Eur. J. Cell Biol. 89, 674–680.

van den Dries, K., Meddens, M.B., de Keijzer, S., Shekhar, S., Subramaniam, V., Figdor, C.G., and Cambi, A. (2013). Interplay between myosin IIA-mediated contractility and actin network integrity orchestrates podosome composition and oscillations. Nat. Commun. 4, 1412.

van Helvert, S., Storm, C., and Friedl, P. (2018). Mechanoreciprocity in cell migration. Nat. Cell Biol. 20, 8–20.

Vogel, V., and Sheetz, M. (2006). Local force and geometry sensing regulate cell functions. Nat. Rev. Mol. Cell Biol. 7, 265–275.

Wisdom, K., and Chaudhuri, O. (2017). 3D cell culture in interpenetrating networks of alginate and rBM matrix. Methods Mol. Biol. 1612, 29–37.

Wisdom, K.M., Adebowale, K., Chang, J., Lee, J.Y., Nam, S., Desai, R., Rossen, N.S., Rafat, M., West, R.B., Hodgson, L., and Chaudhuri, O. (2018). Matrix mechanical plasticity regulates cancer cell migration through confining microenvironments. Nat. Commun. 9, 4144.

Wisdom, K.M., Indana, D., Chou, P.E., Desai, R., Kim, T., and Chaudhuri, O. (2020). Covalent cross-linking of basement membrane-like matrices physically restricts invasive protrusions in breast cancer cells. Matrix Biol. 85–86, 94–111.

Yu, M., Yuan, X., Lu, C., Le, S., Kawamura, R., Efremov, A.K., Zhao, Z., Kozlov, M.M., Sheetz, M., Bershadsky, A., and Yan, J. (2017). mDia1 senses both force and torque during F-actin filament polymerization. Nat. Commun. 8, 1650.

STAR★METHODS

KEY RESOURCES TABLE

REAGENT or RESOURCE	SOURCE	IDENTIFIER
Antibodies		
Monoclonal β1 integrin blocking antibody	Abcam	Cat# ab24693; RRID: AB_448230
Bacterial and virus strains		
DH5alpha Competent Cells	Invitrogen/Thermofisher Scientific	Cat# 18265017
Biological samples		
Viscoplastic interpenetrating network (IPN) hydrogels	Wisdom et al., 2018	N/A
Chemicals, peptides, and recombinant proteins		
Y27632	Sigma Aldrich	Cat# Y0503
Blebbistatin	Abcam	Cat# Ab120425
High glucose Dulbecco's Modified Eagle Medium	Hyclone	Cat# SH30243.01
Fetal Bovine Serum	Hyclone	Cat# SH30071.03HI
Penicillin/Streptomycin	Life Technologies	Cat# 15070063
FluoroBrite	ThermoFisher Scientific	Cat# A1896701
GlutaMAX	ThermoFisher Scientific	Cat# 35050061
0.05% Trypsin/EDTA	ThermoFisher Scientific	Cat# 25300054
Piggybac vector	Gift from A. Dunn	N/A
Alginate	FMC Biopolymer	Pronatal LF 20/40, High-MW. 280 kDa
Matrigel	Corning	Cat# 354230
Calcium Sulfate (CaSO4)	Sigma Aldrich	Cat# 255696-10G
Lipofectamine 3000	ThermoFisher Scientific	Cat# L3000075
OptiMEM	ThermoFisher Scientific	Cat# 31985062
EGF	Peprotech, Inc.	Cat# AF-100-15
Puromycin	ThermoFisher Scientific	Cat# A1113803
Neomycin	ThermoFisher Scientific	Cat# 21810031
Fluoresceinamine	Sigma Aldrich	Cat# 20162
Critical commercial assays		
MycoAlert Mycoplasma Detection Kit	Lonza	Cat# LT07-118
GeneJet Plasmid Miniprep kit	ThermoFisher Scientific	Cat# K0701
Deposited data		
Measured invadopodia dynamics of MDA-MB-231	This paper	https://doi.org/10.17632/tp7fkkxk44.2
Measured circularity of HT-1080 cells	Wisdom et al., 2018	https://doi.org/10.17632/tp7fkkxk44.2
Experimental models: Cell lines		
MDA-MB-231	ATCC	ATCC® HTB-26
HT-1080 cells	ATCC	ATCC® CCL-121
Recombinant DNA		
RFP-LifeAct	Gift from A. Dunn	N/A
Software and algorithms		
Simulation of invadopodia dynamics	This paper	N/A
High throughput invadopodia dynamics analysis	Chang et al., 2020	N/A
MATLAB	Mathworks	https://www.mathworks.com/products/matlab.html
Imaris	Oxford Instruments	https://imaris.oxinst.com/
ImageJ	ImageJ	https://imagej.net/Welcome

(Continued on next page)

Continued		
REAGENT or RESOURCE	SOURCE	IDENTIFIER
Other		
Stress-controlled rheometer	TA Instruments	AR2000EX

RESOURCE AVAILABILITY

Lead contact
Further information and requests for resources and reagents should be directed to and will be fulfilled by the Lead Contact, Vivek B. Shenoy (vshenoy@seas.upenn.edu).

Materials availability
This study did not generate new unique materials.

Data and code availability
Original data have been deposited to Mendeley Data: https://doi.org/10.17632/tp7fkkxk44.2. Codes are available upon request from the corresponding author.

EXPERIMENTAL MODEL AND SUBJECT DETAILS

Cell culture
Human breast adenocarcinoma cells MDA-MB-231 (ATCC) were cultured in high glucose Dulbecco's Modified Eagles Medium (Hyclone) with 10% Fetal Bovine Serum (Hyclone) and 1% Penicillin/Streptomycin (Pen/Strep, Life Technologies) and cultured at 37°C in 5% CO_2. MDA-MB-231 cells were stably transfected to express RFP-LifeAct using a Piggybac vector construct with Geneticin resistance, as described previously (Wisdom et al., 2018). MDA-MB-231 cells were authenticated by ATCC and tested mycoplasma negative.

Preparation of viscoplastic gels
Sodium alginate rich in guluronic acid blocks and with a high molecular weight (FMC Biopolymer, Protanal LF 20/40, High-MW, 280 kDa) was prepared as described previously (Rowley et al., 1999). High-MW was irradiated 3 or 8 Mrad (3 or 8x10^6 rad) by a cobalt source to produce medium-MW (70 kDa) and low-MW (35 kDa) alginates (Chaudhuri et al., 2016). Fluorescein-coupled alginate was prepared by coupling Fluoresceinamine Isomer (Acros Organics) to low-MW alginate using carbodiimide chemistry at a concentration of 37.74 μM. Alginate was dialyzed against deionized water for 3-4 days (MW cutoff at 3,500 Da), treated with activated charcoal, sterile filtered, lyophilized, and then reconstituted in serum-free DMEM (Life Technologies).

The reconstituted basement membrane (rBM) network presents cells with ligands such as laminin and type IV collagen that are typically found in BM, while the tunable alginate network provides control over mechanical properties. The rBM and alginate were mixed and crosslinked with calcium ions to form IPN hydrogels with a final concentration of 4 mg mL^{-1} rBM and 10 mg mL^{-1} alginate. Alginate molecular weight (MW) and cross-linker concentration were varied in order to form a set of IPNs with initial elastic moduli of around 1.8 kPa but varying mechanical plasticity (Wisdom et al., 2018). In addition, calcium crosslinking of the alginate matrix was varied to form a set of IPNs with different elastic moduli, i.e., low stiffness 0.4 kPa (LS), medium stiffness 1.5 kPa (MS), high stiffness 4.4 kPa (HS), and very high stiffness 9.3 kPa (VHS) (Chang et al., 2020).

METHOD DETAILS

Model formulation
Based on Equations 1, 2, 3, and 4 in the Results section, we can obtain the following four ordinary differential equations (ODEs):

$$\frac{R_0}{AE_c}\left(\zeta_r + \frac{F_M}{V_0} + \frac{A\eta_c}{R_0}\right)\frac{dR}{dt} + R = R_0\frac{\zeta_r V_p}{AE_c} - \frac{F_M R_0}{AE_c}\left(1 - \frac{V_p}{V_0}\right) - \frac{F_e R_0}{AE_c}, \tag{5}$$

$$\tau_m\frac{dF_M}{dt} + F_M = F_{M0} + \alpha\zeta_r\left(V_p - \frac{dR}{dt}\right) - \beta\zeta_r\frac{dR}{dt} + \chi_m(t), \tag{6}$$

$$\frac{dF_e}{dt} = \frac{AE_0}{R_0}\frac{dR}{dt} - \frac{E_0}{\eta}\left[\left(1 + \frac{E_1}{E_0}\right)F_e - AE_1\left(\frac{R}{R_0} - \frac{s_p}{R_0}\right)\right] - \frac{AE_0}{R_0}\frac{ds_p}{dt}, \tag{7}$$

$$\frac{ds_p}{dt} = \frac{R_0}{\eta A}\left[F_e - A\sigma_y - \frac{AE_2 s_p}{R_0}\right]H\left(F_e - A\sigma_y - \frac{AE_2 s_p}{R_0}\right). \tag{8}$$

We have four variables: invadopodia length R, maximum force generated by bound myosin F_M, ECM force F_e, and plastic displacement $s_p = R_0\varepsilon_p$. Here $\alpha = \alpha_0 m_0 k_{on}^0/k_{off}$ and $\beta = \beta_0 m_0 f_b/(R_0\zeta_r k_{off})$ are two coefficients characterize effects of the mechano-sensitive signaling pathway on myosin dynamics; $\chi_m(t) = f_b\xi_m(t)/k_{off}$ represents the force fluctuation in myosin dynamics, $F_{M0} = k_{on}^0 m_0 f_b/k_{off}$ is the myosin force equilibrium constant when signaling feedback is absent, $\tau_m = 1/k_{off}$ is the intrinsic myosin recruitment timescale, and $H(x) = \frac{1}{2}\left(1 + \frac{2}{\pi}\arctan\left(\frac{x}{\delta}\right)\right)$ is the Heaviside step function. For details on the model derivation and parameter justification, see Methods S1: Model description, related to STAR Methods and Methods S2: Parameter justification for the model, related to STAR Methods.

Linear stability analysis

Before we perform a linear stability analysis on the equations governing invadopodia dynamics, we take the ECM mechanical response to be elastic with a constant effective modulus $d\sigma/d\varepsilon$ as in the long term, as the cyclic ratcheting of viscoplastic ECM leads to elastic solid behavior (Figures 4A, S1H, S1I, and S2). Thus, the total effective elastic modulus resisting F-actins is given by $E_t = d\sigma/d\varepsilon + E_c$, where E_c is cytoskeleton stiffness. By neglecting the Gaussian noise signal $\chi_m(t)$, the Equations 5, 6, 7, and 8 can be simplified to two ODEs:

$$\frac{R_0}{AE_t}\left(\zeta_r + \frac{F_M}{V_0} + \frac{A\eta_c}{R_0}\right)\frac{dR}{dt} + R = R_0\frac{\zeta_r V_p}{AE_t} - \frac{F_M R_0}{AE_t}\left(1 - \frac{V_p}{V_0}\right), \tag{9}$$

$$\tau_m\frac{dF_M}{dt} + F_M = F_{M0} + \alpha\zeta_r V_p - (\alpha + \beta)\zeta_r\frac{dR}{dt}. \tag{10}$$

When the time derivatives vanish, we can obtain the invadopodia length R_s and the myosin stall force F_{Ms} at the steady state. By applying a small perturbation of δR_s and δF_{Ms} to the steady state, we obtain the Jacobian matrix **J** with eigenvalues $\lambda_{1,2}$:

$$\lambda_{1,2} = \frac{1}{2\tau_e}\left[\left(\frac{\tau_s}{\tau_m} - \frac{\tau_e}{\tau_m} - 1\right) \pm \sqrt{\left(\frac{\tau_s}{\tau_m} - \frac{\tau_e}{\tau_m} - 1\right)^2 - 4\frac{\tau_e}{\tau_m}}\right]. \tag{11}$$

Here τ_m, τ_e and τ_s are the timescales characterizing intrinsic myosin recruitment (without signaling feedback), polymerization-associated extension, and signaling-associated myosin recruitment, respectively, which can be written as:

$$\tau_m = \frac{1}{k_{off}}, \quad \tau_e = \frac{\zeta_r}{k_t} + \frac{\eta_c}{E_t} + \frac{F_{Ms}}{k_t V_0}, \quad \tau_s = (\alpha + \beta)\frac{\zeta_r}{k_t}\left(1 - \frac{V_p}{V_0}\right). \tag{12}$$

Here $k_t = E_t A/R_0$ and $F_{Ms} = F_{M0} + \alpha\zeta_r V_p$ are the effective stiffness (sensed by invadopodia tip) and maximal force of bound myosin in the steady state, respectively. The timescale for intrinsic myosin recruitment τ_m is estimated as $\tau_m \sim 400\,s$; the timescales τ_e and τ_s are estimated to be $\sim 10^3$ s for the oscillatory invadopodia. The eigenvalues $\lambda_{1,2}$ in Equation 11 allow us to determine the dynamic patterns (i.e., oscillatory or monotonically growing) of invadopodia. For details on linear perturbation analysis, see Methods S3: Linear stability analysis, related to STAR Methods

Simulation procedure

The model was implemented using an ODE solver (ode45) in MATLAB (MathWorks). Two event functions were defined in the option structure of ode45 to determine the key events when an invadopodium detaches and re-attaches to the ECM. The detailed model algorithm is described below with the flowchart shown in Figure S3:

(1) Initialize an invadopodium with a length R_0 in contact with undeformed ECM.
(2) Using the ODE solver to solve the Equations 5, 6, 7, and 8
(3) Decide whether the invadopodium detaches itself from the ECM (i.e., the ECM force decreases to zero).

If true, store the invadopodium length R_E (ECM position) and go to step 4.
If not, go to step 6.

(4) Set the ECM force to zero and solve the force balance and myosin dynamics ODEs without ECM resistance force.

(5) Decide whether the invadopodium re-attaches to the ECM (i.e., invadopodium length becomes larger than the previous detachment length R_E).

If true, the invadopodium re-attaches to the ECM, go to step 2.
If not, go to step 6.

(6) The simulation time reaches its final time, end the simulation.

Mechanical characterization

Mechanical plasticity of different alginate-rBM IPN hydrogels was determined using an AR2000EX stress-controlled rheometer (TA Instruments). IPNs, made for mechanical testing as described previously (Chaudhuri et al., 2014; Wisdom et al., 2018), were deposited onto a flat steel rheometer stage fitting immediately after mixing with crosslinker. A 25 mm flat plate fitting was then immediately brought down, forming a 25 mm gel disk. The storage and loss moduli at 1 rad/s and 1% strain, a frequency and amplitude which were both within linear regimes, were recorded for at least 2 hours in order to verify gelation and equilibration of hydrogel mechanical properties. To quantify mechanical plasticity, this time sweep was followed by a creep-recovery test. This involved first applying constant shear stress (100 Pa) for 1 hour while strain was recorded as a function of time. Then, the sample was unloaded (0 Pa), and strain was recorded as a function of time as the sample recovered from the absence of load for 6,400 s (1.7 hours). This recovery time period was sufficient to minimize transient effects due to stress unloading.

To perform repeated creep recovery tests, the ECM was loaded with constant shear stress (50 Pa) for 10 minutes, while the strain was recorded as a function of time. The load was then removed (0 Pa), and strain was recorded as a function of time for 10 minutes. This cycle of 10 minutes of loading (creep) and 10 minutes of unloading (recovery) was repeated 10 times for the ECM. This repeated loading-unloading cycle mimics the periodic nature of invadopodia protrusions discussed in the current study. Furthermore, the 10-minute recovery period was sufficient to minimize transient effects due to repeated loading-unloading, and is on a similar time-scale as the invadopodia structure discussed in this study. For details on the fitting for the creep recovery tests, see Methods S4: Fitting for the mechanical tests, related to STAR Methods.

3D cell encapsulation in IPNs

For time-lapse invadopodia extension studies, MDA-MB-231 were starved overnight in serum-free medium and then encapsulated in IPNs similar to what has been described previously (Chaudhuri et al., 2014; Wisdom and Chaudhuri, 2017; Wisdom et al., 2018). Cells were then washed with PBS, trypsinized using 0.05% trypsin/EDTA, washed, centrifuged, and resuspended in serum-free medium. The concentration of cells was determined using a Vi-Cell Coulter counter (Beckman Coulter). After Matrigel was mixed with alginate, cells were added into this polymer mixture and deposited into a cooled syringe. The solution was then vigorously mixed with a solution containing $CaSO_4$ and deposited into wells of a chambered coverglass (LabTek). The final concentration of cells was 2×10^6 cells/mL IPN. The cell-laden hydrogels gelled in an incubator at 37°C and 5% CO_2 for 35-45 minutes. After IPN gelation, starvation medium was added which contained FluoroBrite (ThermoFisher Scientific) supplemented with GlutaMAX (ThermoFisher Scientific) and 1% Pen/Strep, with vehicle alone or inhibitor. One day later, starvation medium was removed and 60 μL of a 0.75% agarose (Sigma-Aldrich) hydrogel was added to each well to hold the IPN in place along with the invasion medium (FluoroBrite supplemented with GlutaMAX, 1% Pen/Strep, 15% FBS, 50 ng/mL EGF, and either vehicle or inhibitor). Cells were then imaged live in an incubated chamber (37°C and 5% CO_2) at 20-minute intervals with a Leica HCX PL APO 10X/0.40 NA objective overnight. ImageJ was used to identify and characterize length of protrusions over time.

For matrix visualization studies, RFP-LifeAct MDA-MB-231 cells were similarly encapsulated in IPNs formed using fluorescein-conjugated alginate, and imaged live at 20-minute intervals using a Leica HC PL APO 63X/1.4 NA oil immersion objective.

Blocking antibody and inhibitor experiments

Inhibitors were implemented into time-lapse protrusion extension studies as follows: 10 μM Y27632 to inhibit ROCK (Sigma-Aldrich), 1 μg/mL monoclonal β1 integrin blocking antibody (Abcam, P5D2), and 50 μM Blebbistatin (Abcam).

High-throughput invadopodia dynamics analysis

Images acquired from confocal imaging of RFP-LifeAct transfected MDA-MB-231 cells were imported into Imaris (Bitplane), a commercially available software that enables 3D and 4D volume rendering and analysis. Surface renderings using the RFP channel were performed for high throughput invadopodia dynamics analysis. Translational drift was corrected for all images. Poorly segmented cells and partially imaged cells at frame edges were excluded. Further details can be referred to one previously published work (Chang et al., 2020). Objected-oriented bounding box lengths for each cell was exported from Imaris and analyzed with custom MATLAB code, and three box lengths a, b and c (note $a \geq b \geq c$) for three principal axes can be obtained (Figure S5A). The length of the invadopodia was calculated as $l_{invad} = a - (b + c)/2$. To extract the amplitude of invadopodia oscillation, we converted experimental data from time domain to frequency domain using Fast Fourier Transformation (FFT). The oscillation amplitude was calculated by averaging the highest three peaks in the frequency domain (Figures S5C-S5D).

QUANTIFICATION AND STATISTICAL ANALYSIS

Statistical analyses were performed using MATLAB (MathWorks), and data were compared using the one-way ANOVA with Benjamini-Hochberg Procedure or Mann-Whitney U-test as indicated in figure legends. The error bars in Figures 1 and S1 represent standard deviation (SD), and the error bars in Figures 4, 5, S6, and S9 indicate 95% confidence intervals. The sample sizes and p values are given in the figures and figure legends.